Geophys. J. Int. (2016) **204,** 719–735
GJI Seismology

doi: 10.1093/gji/ggv457

Sequencing of tsunami waves: why the first wave is not always the largest

Emile A. Okal[1] and Costas E. Synolakis[2,3]

[1] *Department of Earth & Planetary Sciences, Northwestern University, Evanston, IL* 60201*, USA. E-mail:* emile@earth.northwestern.edu
[2] *Department of Civil and Environmental Engineering, University of Southern California, Los Angeles, CA* 90089*, USA*
[3] *School of Environmental Engineering, Technical University of Crete, GR-*73100 *Chania, Greece*

Accepted 2015 October 19. Received 2015 October 18; in original form 2015 April 17

SUMMARY

This paper examines the factors contributing to the 'sequencing' of tsunami waves in the far field, that is, to the distribution of the maximum sea surface amplitude inside the dominant wave packet constituting the primary arrival at a distant harbour. Based on simple models of sources for which analytical solutions are available, we show that, as range is increased, the wave pattern evolves from a regime of maximum amplitude in the first oscillation to one of delayed maximum, where the largest amplitude takes place during a subsequent oscillation. In the case of the simple, instantaneous uplift of a circular disk at the surface of an ocean of constant depth, the critical distance for transition between those patterns scales as r_0^3 / h^2 where r_0 is the radius of the disk and h the depth of the ocean. This behaviour is explained from simple arguments based on a model where sequencing results from frequency dispersion in the primary wave packet, as the width of its spectrum around its dominant period T_0 becomes dispersed in time in an amount comparable to T_0, the latter being controlled by a combination of source size and ocean depth. The general concepts in this model are confirmed in the case of more realistic sources for tsunami excitation by a finite-time deformation of the ocean floor, as well as in real-life simulations of tsunamis excited by large subduction events, for which we find that the influence of fault width on the distribution of sequencing is more important than that of fault length. Finally, simulation of the major events of Chile (2010) and Japan (2011) at large arrays of virtual gauges in the Pacific Basin correctly predicts the majority of the sequencing patterns observed on DART buoys during these events. By providing insight into the evolution with time of wave amplitudes inside primary wave packets for far field tsunamis generated by large earthquakes, our results stress the importance, for civil defense authorities, of issuing warning and evacuation orders of sufficient duration to avoid the hazard inherent in premature calls for all-clear.

Key words: Numerical solutions; Tsunamis; Pacific Ocean.

1 INTRODUCTION

The scope of this paper is to understand under which conditions the maximum amplitude of a tsunami at a receiving shore in the far field may or may not occur as part of the first-arriving wave.

We are motivated in this respect by the experience of the first author (EAO) during the 2011 Tohoku tsunami, when he was a participant in the tsunami warning issued for French Polynesia, which resulted in the evacuation of low-lying areas in the city of Papeete, Tahiti. As documented in Reymond *et al.* (2013), from which Fig. 1 is reproduced, the largest wave in Papeete harbour turned out to be the fourth one, occurring 72 min after the first-arriving wave. As a result, the all clear which had been broadcast to allow residents to return to their houses and businesses had to be canceled, leading to an episode of significant confusion among the population.

This occurrence is far from unique. We recall, for example, the case of the 1960 Chilean tsunami in Hilo, Hawaii. As detailed by Eaton *et al.* (1961), the first wave, arriving at midnight local time, featured an amplitude of only 1.2 m, while the maximum of 5 m was reached one hour later, after an all clear had been issued by the local authorities; it resulted in 61 casualties in Hilo. Similarly, during the 1964 'Good Friday' Alaskan tsunami, in the coastal city of Crescent City, California, some of the 11 victims were killed after they 'prematurely returned to the evacuation area following the first relatively mild waves, because they thought the danger had passed' (National Research Council 1970).

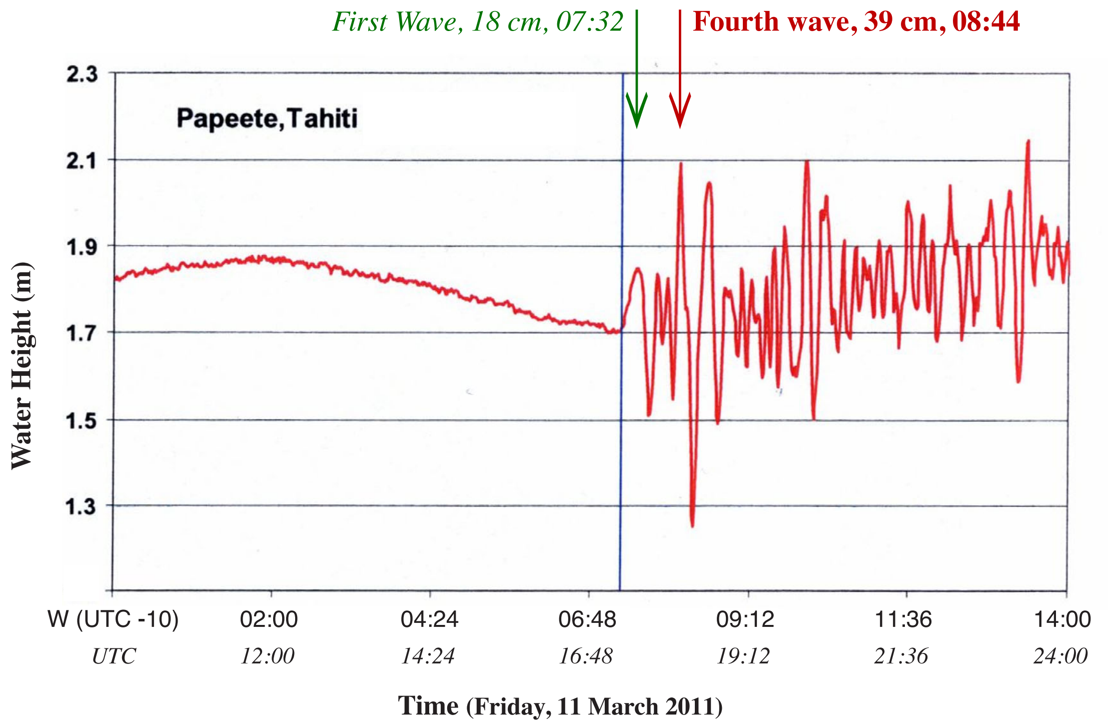

Figure 1. Maregram of the 2011 Tohoku tsunami at Papeete, Tahiti. Note that the maximum amplitude is carried by the fourth wave, 72 min after the first one (after Reymond *et al.* 2013).

We do not consider here the physically different case of significantly higher frequency components to the tsunami wave, typically in the 10 mHz frequency range (or at periods of a few minutes), which can set harbours and bays in resonance, thus reaching extreme values for wave amplitude or current velocities, as exemplified in Toamasina, Madagascar during the 2004 Sumatra tsunami (Okal *et al.* 2006), or in Puamau, Marquesas Islands during the 2010 Chilean event (Reymond *et al.* 2013). Such high-frequency waves, traveling outside the shallow-water approximation (SWA), can feature delays of many hours (up to 7 in the case of Toamasina) when propagating across major oceanic basins. Rather, we limit ourselves to the case of waves comprising the first packet, broadly interpreted as traveling under the SWA or very closely thereafter, but featuring several oscillations whose time separation does not exceed one to two hours, as shown in Fig. 1. Even in a lower frequency range, some harbours can feature resonant periods comparable to those of main tsunami waves (e.g. 22 min (0.75 mHz)) at Crescent City, which may lead to the amplification of later arrivals, as well as the development of very strong currents (e.g. Admire *et al.* 2014). We will use the model of an ocean of constant depth without any shores to eliminate such effects, and thus focus on the influence of source and propagation on the evolution of wave amplitudes.

In order to ease the language, we will refer to the question of which wave carries the largest amplitude in a far-field tsunami as *'sequencing'* of the wave packet; a scenario in which the first wave carries the maximum amplitude will be called an *'MF'* wave (for 'Maximum First'; Fig. 2a) as opposed to an *'MD'* wave (for 'Maximum Delayed'; Fig. 2b) when the maximum amplitude is carried by a later arrival.

It is well known that the question of the structure of a far-field tsunami wave, and hence presumably of its sequencing, is a very complex function of many successive factors in its development: the characteristics—size and geometry—of the parent earthquake, the effect of the irregular bathymetry of the ocean basin (which can e.g. lead to multipathing and focusing or defocusing), and finally the fundamentally non-linear response of the individual site (shore, bay or harbour) where the wave is recorded. Here, we seek an understanding to the question of which one(s) among these parameters may control sequencing, and in particular the development of *MD* patterns.

The last effect, that is, the role of shorelines, may be eliminated by considering records obtained by DART sensors on the high seas, unaffected by the response of coastal structures. For this purpose, we have gathered all available DART buoy records in the Pacific Basin of the 2010 Maule and 2011 Tohoku tsunamis. On Figs 2(a) and (b), we show examples of *MF* and *MD* records from the Tohoku tsunami. This establishes that variations in sequencing are not (at least not entirely) due to coastal response, but rather are already present in the various far-field wave packets propagating on the high seas. Figs 2(c) and (d) attempt to map the repartition of *MF* and *MD* records. This is made difficult by the relative scarcity of DART systems in the Pacific Basin, especially given the many stations which were not operational during the 2010 Maule tsunami. Notwithstanding these reservations, these maps would tentatively suggest that *MD* records develop preferentially at greater distances, and in the lobe of radiation perpendicular to faulting (in this respect, we dismiss the case of the *MD* records developed in 2011 in the lee of the Alaskan Peninsula, as they most probably result from complex propagation skirting the Aleutian Islands, rather than along the plotted great circles).

In Section 2, we use numerical simulations to reproduce the onset of *MD* records based on a number of simple models, in an attempt to eliminate spurious parameters, and to define the physical origin of the sequencing phenomenon. We conclude that its root lies in frequency dispersion arising in the vicinity of, but immediately outside, the SWA. By using theoretical models with oceans of constant depth, we can eliminate the influence of refraction, which has been shown to occasionally lead to focusing of energy into later arrivals

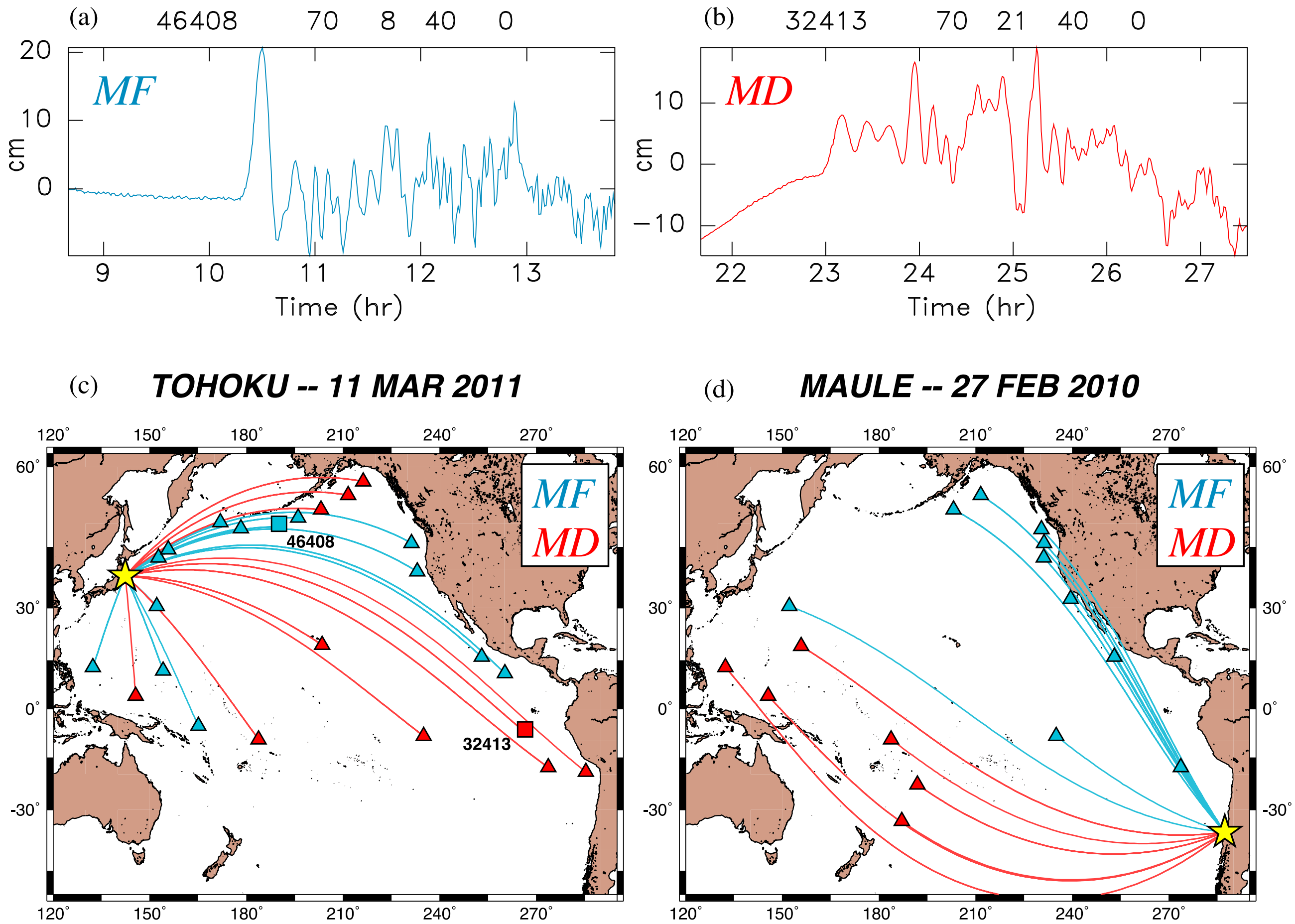

Figure 2. (a) Example of an *'MF'* wave, in which the maximum amplitude is achieved by the first wave, as recorded by DART buoy number 46408 (blue square in (c)) during the 2011 Tohoku tsunami. (b) Example of *'MD'* wave, in which the maximum is carried by a later arrival, as recorded by DART buoy 32413 (red square in (c)) during the Tohoku tsunami. (c) Map of DART records available for the 2011 Tohoku tsunami, colour-coded according to sequencing (blue for *MF* paths; red for *MD* ones). Ray paths are idealized as great circles, rather than actual paths resulting from irregular bathymetry and the presence of continental and island structures. (d) Same as (c) for the 2010 Maule, Chile tsunami.

which may feature larger amplitudes than initial ones (e.g. Kowalik *et al.* 2005; Rabinovich *et al.* 2011; Titov *et al.* 2005). Similarly, our approach excludes the potential effect of reflection by prominent bathymetric features such as large islands or oceanic plateaux, which can lead to large-amplitude delayed arrivals, as described, for example, by Shevchenko *et al.* (2013) at Severo Kuril'sk during the 2010 Chilean tsunami.

In Section 3, we apply this concept and confirm our results in the real-life cases of realistic earthquake-generated tsunamis, and further document the influence played by irregular bathymetry on the transition from *MF* to *MD* regimes.

2 SEQUENCING IN CLASSICAL ANALYTICAL SOLUTIONS

In order to gain as much insight as possible into the origin of sequencing, we first work on simple cases for which analytical solutions are available. We use the model of an ocean of constant depth h, which eliminates any possible effect of multipathing and refraction due to lateral heterogeneity in propagation. The curvature of the Earth is neglected and the medium has no lateral limits.

2.1 Le Méhauté & Wang's (1995) formalism

We start by considering the approach of Le Méhauté & Wang (1995; hereafter LMW), who expand the solution of a linear irrotational wave propagating from a finite disturbance with axial symmetry as

$$\eta(r,t) = \int_0^{\infty} k \cdot J_0(kr) \cdot \mathbf{H}(k) \cdot \cos \omega t \;\; dk, \tag{1}$$

where ω is the angular frequency of the spectral component with wavenumber k:

$$\omega^2 = gk \cdot \tanh(kh), \tag{2}$$

J_ν the Bessel function of first kind and order ν and $\mathbf{H}(k)$ is the Hilbert transform of the initial displacement of the water surface at the origin time $t = 0$:

$$\mathbf{H}(k) = \int_0^{\infty} \eta(r', 0) J_0(kr') r' dr'. \tag{3}$$

We consider here a 'top hat' distribution

$$\eta(r', 0) = \eta_0 \cdot H(r_0 - r'), \tag{4}$$

where H is the Heaviside function. This model describes the instantaneous uplift (by an amount η_0) of a circular plug of radius

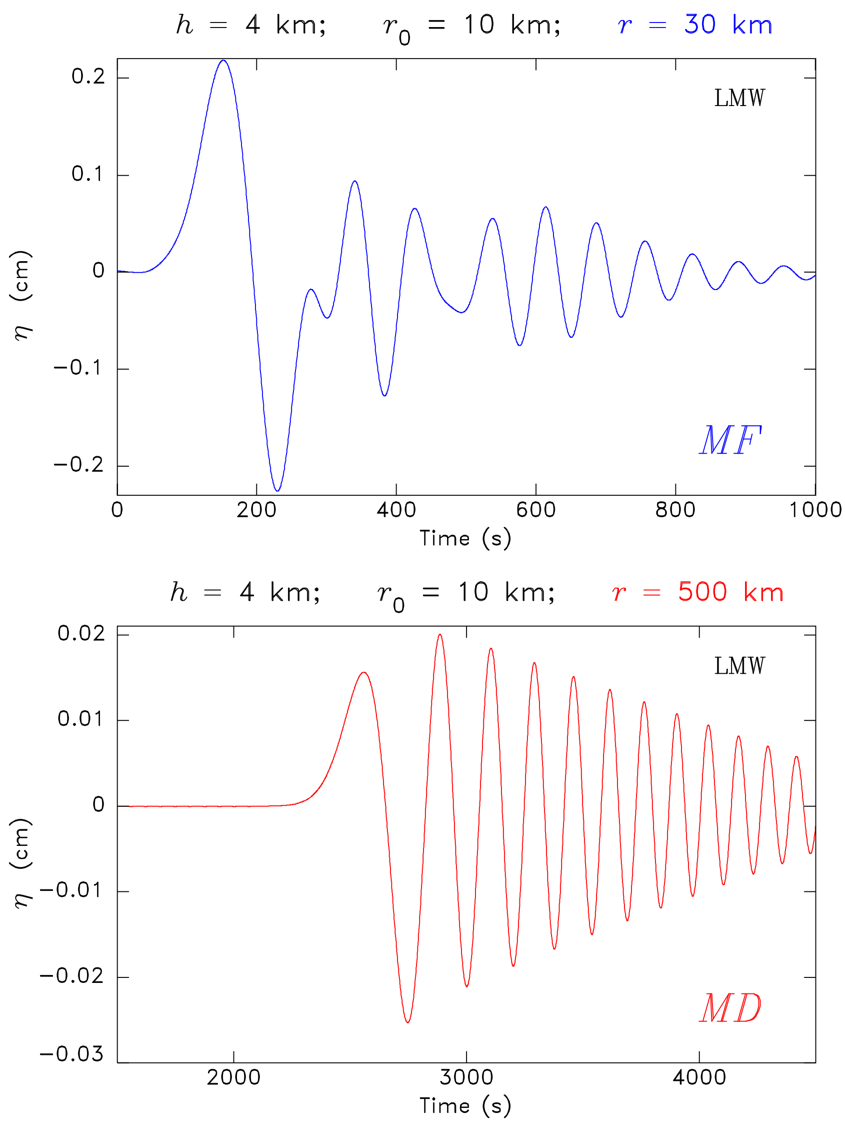

Figure 3. Examples of waveshapes synthesized from eq. (5) (Le Méhauté and Wang 1995) at short and large distances (30 km, top, and 500 km, bottom, respectively). Note the transition from *MF* to *MD* patterns.

r_0 at time $t = 0$. Substituting (4) into (3) leads to the general solution

$$\eta(r,t) = \eta_0 \cdot r_0 \int_0^\infty J_0(kr) J_1(kr_0) \cdot \cos \omega t \, dk. \tag{5}$$

Note that because of the existence of two independent scaling lengths in the problem (namely the radius r_0 of the plug and the depth h of the oceanic column) and of the non-linearity of the dispersion relation (2), eq. (5) does not lend itself to simple non-dimensionalization and the evolution of sequencing is not expected to be simply a function of r/r_0.

Note also that our approach differs from that of previous investigators, (e.g. Kajiura 1963), who considered the more complex (but admittedly more realistic) case of a rectangular fault, and who was primarily concerned with the evolution of maximum amplitude η with range r, irrespective of the problem of sequencing.

On Fig. 3, we present two examples of waveforms η obtained by numerically computing eq. (5) at distances $r = 30$ and 500 km for the following parameters: $h = 4$ km; $r_0 = 10$ km; $\eta_0 = 1$ cm. This figure clearly establishes the former as an *MF* wave, and the latter as an *MD* one. Note on this figure that, as predicted by the *N*-wave model of Tadepalli & Synolakis (1996), sequencing does not affect the *polarity* of the first arriving waves (a leading elevation in both cases); only the distribution of amplitude among subsequent waves is affected.

A more systematic variation of the range r confirms the trend and establishes that the transition, when the first and second waves have equal amplitudes, occurs at a critical range $r_c = 135$ km. We generalize these results by first varying r_0, the other parameters remaining constant. Fig. 4 gives a summary of the results, colour-coded according to sequencing (*MF* wave trains in blue; *MD* ones in red). Note that for all values of r_0, the evolution of sequencing is from *MF* patterns at short distances to *MD* ones at greater distances. The critical distance r_c (open symbols on Fig. 4) can be approximated by its regression as a function of r_0:

$$\log_{10} r_c^{(4)} = 3.243 \log_{10} r_0 - 1.105, \tag{6}$$

where r_c and r_0 are in km and the superscript $^{(4)}$ refers to the case of a 4-km depth ocean; the rms residual is $\sigma^{(4)} = 0.02$ logarithmic units.

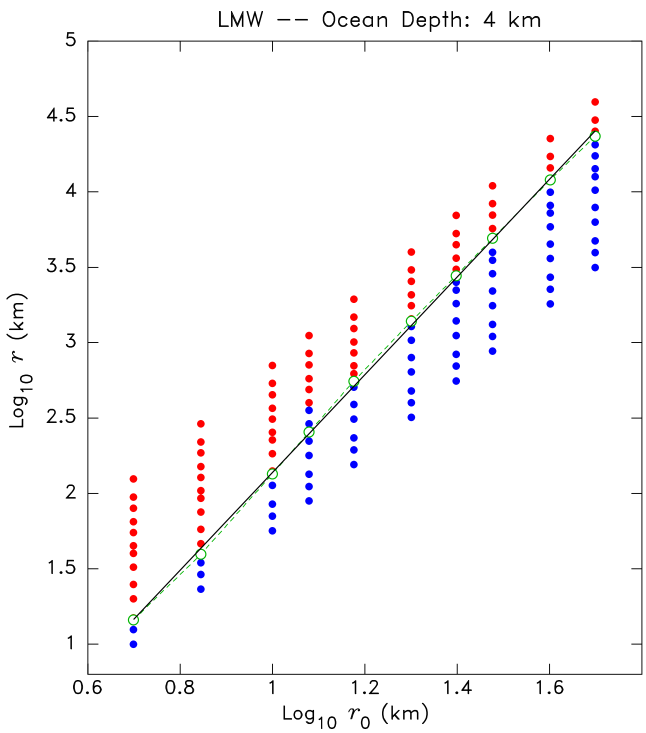

Figure 4. Summary of sequencing of LMW solutions (5), for $h = 4$ km. For each combination of r_0 and r, a colour-coded dot (*MF* in blue; *MD* in red) is plotted using logarithmic coordinates. The open symbols (linked by the dashed line) represent for each value of r_0 the critical range r_c at which the character of sequencing changes from *MF* to *MD*. The straight line is the best linear fit (6) to $\log_{10} r_c$ versus $\log_{10} r_0$.

The influence of the depth of the ocean is examined on Fig. 5(a), where the depth h has been halved ($h = 2$ km). The new regression,

$$\log_{10} r_c^{(2)} = 3.174 \log_{10} r_0 - 0.357 \tag{7}$$

($\sigma^{(2)} = 0.02$), has a slightly less steep slope than (4), which suggests that, while r_c is very roughly multiplied by 4 from the case $h = 4$ km, the increase is not strictly linear, with ratios varying from 4.6 for small r_0 to 4.1 around 30 km. Note that in this case, we restrict r_0 to a maximum of 30 km, since the corresponding r_c becomes larger than 25 000 km. Similarly, we consider on Fig. 5(b) the case of a hypothetical ocean with double the standard depth, $h = 8$ km. While this is obviously unrealistic in the real Earth, it can help shed some general light on the dependence of sequencing on h. Again, the regression

$$\log_{10} r_c^{(8)} = 2.836 \log_{10} r_0 - 1.194 \tag{8}$$

has a gentler slope than (6), but the curvature is clearly more important ($\sigma^{(8)} = 0.15$) with ratios $r_c^{(8)}/r_c^{(4)}$ varying from 0.24 at $r_0 = 50$ km to 0.86 (practically unchanged) at $r_0 = 5$ km.

These results can be regrouped by fitting the following linear relationship between the logarithms of h, r_0 and r_c (all expressed in km):

$$\log_{10} r_c = 3.063 \log_{10} r_0 - 2.058 \log_{10} h + 0.375, \tag{9}$$

with a global rms value of $\sigma = 0.11$ logarithmic units. From the standpoint of dimensionality, note that the algebraic sum of the slopes in (9) approaches unity, suggesting a dependence of the form

$$r_c = A r_0 \cdot \left(\frac{r_0}{h}\right)^a \tag{10}$$

with $a \approx 2.0$. The simplicity of this result warrants deeper physical understanding.

2.2 A model to explain eq. (10)

Fig. 6 shows spectrograms of the representative time-series shown on Fig. 3, and computed under the LMW formalism. The black curve on each frame expresses the dispersion expected from (2). It is clear that strong dispersion is present in the early phases of the wave train at the larger distance, giving it an *MD* character (and indeed, it was already apparent in the time domain on Fig. 3). By contrast, at the shorter distance featuring an *MF* wave train, dispersion is present, but not readily discernable as it takes place within the first oscillation of the time-series.

This observation provides a very strong hint that sequencing may be controlled by dispersion taking place in the initial phases of the wave train at the distance r_c. Under linear dispersive theory, we write the dispersion as a function of the variable $\xi = kh$:

$$\omega^2 = gk \cdot \tanh(kh) = \frac{g}{h} \cdot \xi \cdot \tanh(\xi) \tag{11}$$

which leads to the following expressions for ω, and the phase and group velocities, c and U:

$$\omega = \sqrt{\frac{g}{h}} \cdot \sqrt{\xi \cdot \tanh \xi} \tag{12}$$

$$c = \frac{\omega}{k} = \omega \frac{h}{\xi} = \sqrt{gh} \cdot \sqrt{\frac{\tanh \xi}{\xi}} \tag{13}$$

$$U = \frac{d\omega}{dk} = \frac{h}{2\omega} \cdot \frac{d(\omega^2)}{d\xi} = \frac{1}{2}\sqrt{gh} \cdot \left[\frac{\tanh \xi + \xi(1 - \tanh^2 \xi)}{\sqrt{\xi \tanh \xi}}\right] \tag{14}$$

Note that (11)–(14) are exact expressions under the linear dispersive theory.

We now take the variable ξ as small ($\xi \ll 1$), but not identically zero (which would be the SWA), and seek the first terms of the Taylor expansion of (11):

$$\omega^2 = \frac{g}{h}\xi \cdot \tanh(\xi) = \frac{g}{h} \cdot \xi^2 \cdot \left(1 - \frac{\xi^2}{3} + \frac{2}{15}\xi^4\right), \tag{15}$$

leading to

$$\omega = \sqrt{\frac{g}{h}} \cdot \xi \cdot \left(1 - \frac{\xi^2}{6} + \frac{\xi^4}{40}\right);$$
$$c = \frac{\omega}{k} = \sqrt{gh} \cdot \left(1 - \frac{\xi^2}{6} + \frac{\xi^4}{40}\right). \tag{16}$$

As for the group velocity U, it is obtained simply from (16)

$$U = \frac{d\omega}{dk} = h\frac{d\omega}{d\xi} = \sqrt{gh} \cdot \left(1 - \frac{\xi^2}{6} + \frac{\xi^4}{40} - \frac{\xi^2}{3} + \frac{\xi^4}{10}\right)$$
$$= \sqrt{gh} \cdot \left(1 - \frac{\xi^2}{2} + \frac{\xi^4}{8}\right). \tag{17}$$

Dispersion is expressed by the variation of group velocity with frequency,

$$\frac{dU}{d\omega} = \frac{dU}{d\xi} \cdot \frac{d\xi}{dk} \cdot \frac{dk}{d\omega} = \frac{h}{U} \cdot \frac{dU}{d\xi}, \tag{18}$$

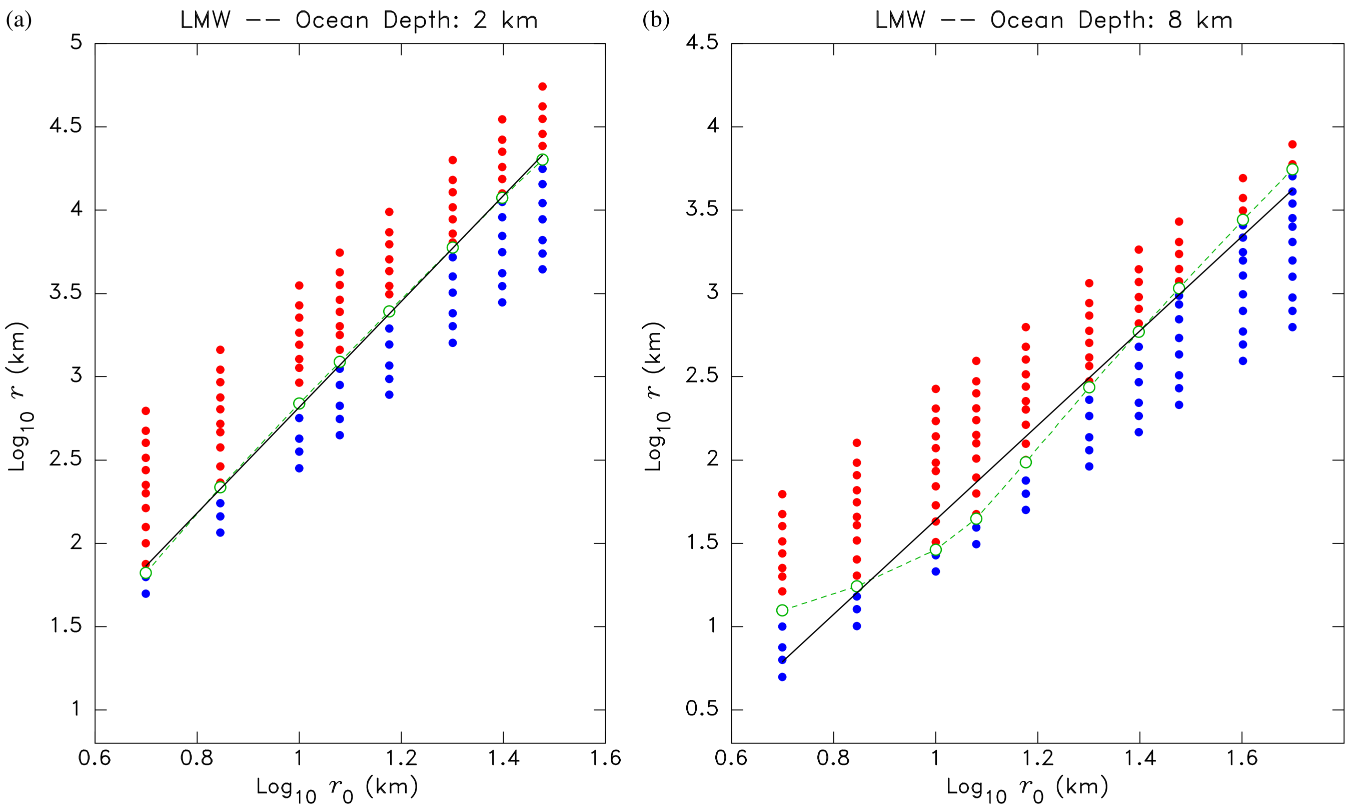

Figure 5. (a) Same as Fig. 4 for the shallower ocean, $h = 2$ km. (b) Same as Fig. 4 for the deeper ocean, $h = 8$ km.

or

$$\frac{dU}{d\omega} = \frac{h}{\sqrt{gh}} \cdot \left(1 + \frac{\xi^2}{2}\right) \cdot \sqrt{gh} \cdot \left(-\xi + \frac{\xi^3}{2}\right)$$
$$= -\xi h + \mathrm{O}\left(\xi^5\right) \approx -kh^2, \tag{19}$$

in itself an extremely simple result.

For propagation to a distance r, the dispersion expressed by (19) results in a *variation of traveltime t* with frequency given by

$$\frac{dt}{d\omega} = -\frac{r}{U^2} \cdot \frac{dU}{d\omega} = -\frac{r}{gh} \cdot \frac{1}{(1-\xi^2/2)^2} \cdot \frac{dU}{d\omega}$$
$$= \frac{r}{g} \cdot \xi \cdot (1 + \xi^2). \tag{20}$$

We then make a number of *ad hoc* assumptions, derived from a phenomenological examination of a large data set of numerical computations of LMW's integral (5):

(i) We assume that the initial wave packet at the distance r_c has a central (angular) frequency ω_0, and that the width of this wave packet is $\Delta\omega$. Note that ω_0 may not necessarily be the frequency corresponding to the absolute maximum spectral amplitude of the full wave train, but rather the dominant frequency in the initial wave packet.

(ii) We assume that sequencing, i.e. the transition from *MF* to *MD*, takes place when the duration of dispersion, taken as the product of (20) by $\Delta\omega$, reaches some fraction β of the main period $2\pi/\omega_0$. This means that r_c should be given by

$$r_c = \frac{2\pi\beta g}{\xi(1+\xi^2) \cdot \Delta\omega \cdot \omega_0}; \quad \text{to first order} \quad r_c = \frac{2\pi\beta g}{\xi_0 \cdot \Delta\omega \cdot \omega_0}. \tag{21}$$

(iii) We further assume that the dominant frequency in the early phases of the wave train, $T_0 = 2\pi/\omega_0$, is related to the time it takes a long wave to transit through the source,

$$T_0 = \gamma \frac{r_0}{\sqrt{gh}}; \qquad \omega_0 = \frac{2\pi}{\gamma} \frac{\sqrt{gh}}{r_0}, \tag{22}$$

where γ is a constant of order 1, which is simply the ratio of the dominant wavelength Λ_0 to r_0.

(iv) Finally, we make the assumption that $\Delta\omega$ is itself proportional to ω_0:

$$\Delta\omega = \delta\omega_0. \tag{23}$$

Combining (21)–(23) leads to the final expression for r_c:

$$r_c = \frac{\beta\gamma^3}{4\pi^2\delta} \cdot \frac{r_0^3}{h^2}, \tag{24}$$

which is exactly the form of eq. (10) with $a = 2$. We have verified that forcing the slopes in regression (9) to their values in (24) (3 and −2) leads to a quality of fit not significantly different from that in (9) where the slopes are not constrained (σ = 0.111 as opposed to 0.109 logarithmic units). We conclude that the data set of critical sequencing distances r_c obtained using the LMW formulation agrees with the simple model described above. It is more difficult to interpret the locking constant obtained from the forced regression (0.414 instead of 0.375 in (9)), which requires

$$\frac{\beta\gamma^3}{4\pi^2\delta} = 2.60, \tag{25}$$

but we note that it remains of order 1, which is generally consistent with our model.

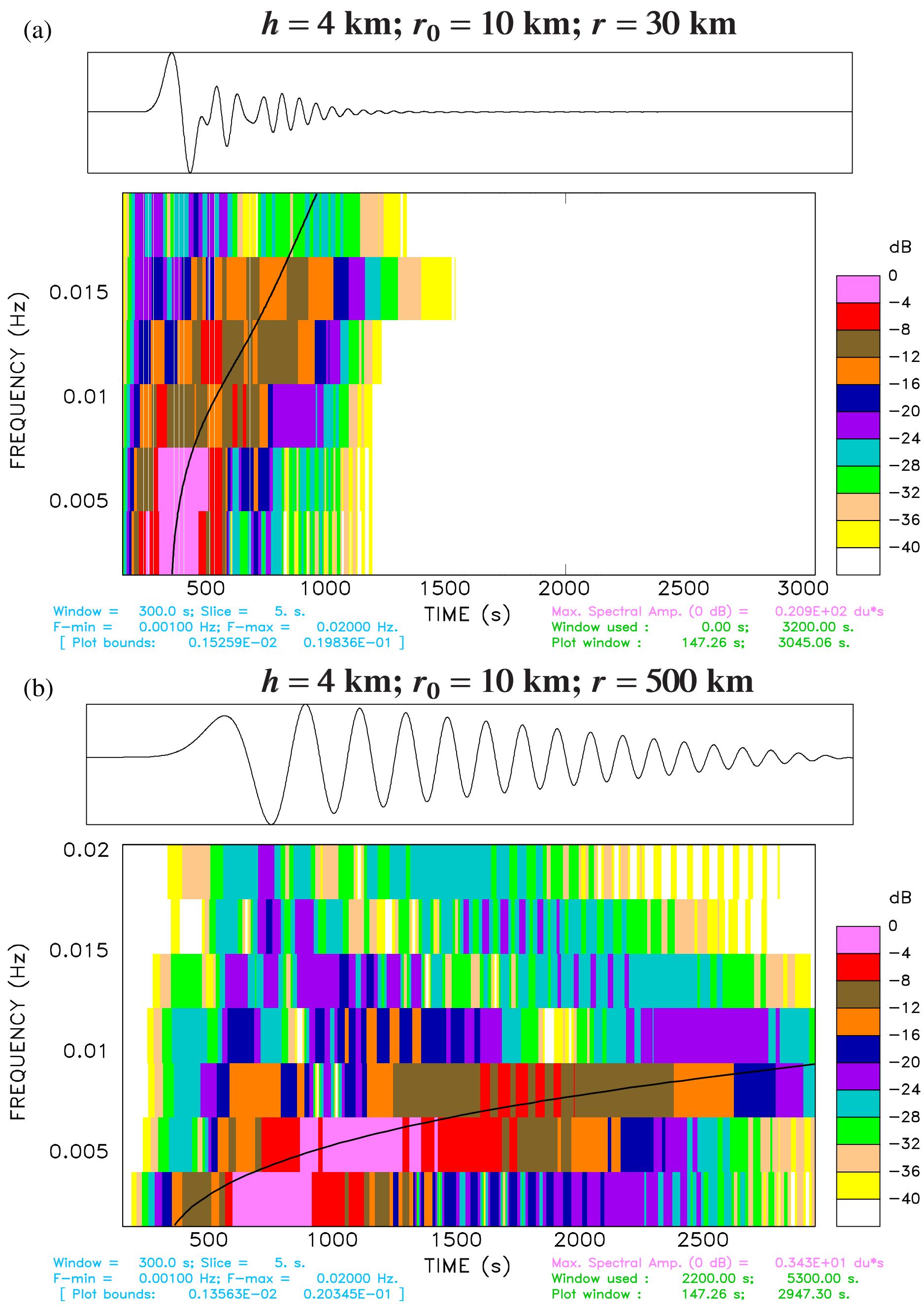

Figure 6. Spectrograms of the wave trains shown on Fig. 3. Top: *MF* wave train at short range ($r = 30$ km). Bottom: *MD* wave train at large range ($r = 500$ km). Note the different timescales on the horizontal axes. In each frame, the solid black line expresses the dispersion expected under eq. (8). Note that while dispersion is present in both frames, it is not directly discernable inside the initial wave packet at the shorter distance.

In order to further verify the general validity of our model, we investigate independently the relationship between ω_0 and the parameters of the source, r_0 and h. For this purpose, we analyse the synthetic records computed using LMW's integral (5) for the three depths $h = 2$, 4, 8 km and for values of r_0 ranging from 5 to 50 km (30 km for $h = 2$ km). For each combination, the computation is made at the critical distance r_c. We define the dominant period in the initial wave packet by considering the first minimum in the time-series (for positive η_0, it is our experience that this is also the absolute minimum of the whole time-series). This minimum occurs at a group time $t_{\min}$, which corresponds to a group velocity $U_{\min} = r_c/t_{\min}$ that can be numerically inverted into a parameter $\xi_{\min}$ using the exact eq. (14), and then into the parameter ω_0 using (11). A double logarithmic regression of a set of 28 such measurements shows that the dominant period $T_0 = 2\pi/\omega_0$ can be approximated by

$$\log_{10} T_0 = 0.944 \log_{10} r_0 - 0.442 \log_{10} h + 1.673 \tag{26a}$$

$$\log_{10} \omega_0 = -0.944 \log_{10} r_0 + 0.442 \log_{10} h - 0.875, \tag{26b}$$

where T_0 is in seconds (ω_0 in rad s^{-1}), r_0 and h in km and with an rms residual $\sigma = 0.05$ logarithmic units.

Note that the regression slopes in eq. (26a) are remarkably close to the values assumed in our model (1 and –0.5, respectively). If the slopes are forced to those values, the best-fitting constant in (26a) becomes 1.643, which in turns leads to $\gamma = 4.3$. This remark provides an *a posteriori* justification of our assumption by suggesting that T_0 may simply be close to the time $4r_0/\sqrt{gh}$ required for a round trip across the circular source plug under the SWA. The expression of the dominant period (26) is also in general agreement with the proportionality of wavelength with source size (e.g. Mirchina *et al.* 1980), even though these authors considered the more complex case of a source of elliptical shape.

Furthermore, our result (24) can be compared to the 'characteristic distance for dispersion' obtained by Mirchina & Pelinovsky (1982, eq. 13), which, when combined with Mirchina & Pelinosky's (1980) scaling of wavelength to source size, takes the form 1.32 r_0^3/h^2, the constant 1.32 being roughly one-half of the ratio (25); this agreement can be regarded as excellent given these authors' cautionary note regarding the selection of the constant, and more generally the fact that a change in sequencing into an *MD* pattern may require a more fully dispersed wave train and hence a greater range r than would the mere observation of dispersion.

2.3 Hammack's (1972) approach

Another, somewhat different, analytical solution to the general problem of the wave propagating from an initial disturbance under axial symmetry was given by Hammack (1972, hereafter JLH). Specifically, his approach considers the problem of the tsunami generated by the uplift (in an amount ζ_0) of a circular plug of radius r_0 on the ocean floor:

$$\zeta(r;t) = \zeta_0(1 - e^{-\alpha t}) \cdot H(t) \cdot H(r_0 - r), \tag{27}$$

where $1/\alpha$ is the time constant of the source and H the Heaviside function. Hammack (1972) used linear dispersive theory to solve the wave equations with (27) as a boundary condition. Note that the finiteness of the coefficient α implies that (27) is not *stricto sensu* an 'initial' condition, the difference becoming meaningful for very small values of α (large values of the rise time); furthermore it will result in a field of 'initial' surface particle velocities which is not identically zero (for any strictly positive time t, even smaller than $1/\alpha$, these velocities will already be non-zero, while the motion of the bottom is still going on). This constitutes a fundamental difference between LMW's approach which uses the initial condition (4) at the surface of the ocean rather than JLH's boundary condition (27) at the bottom, and in this respect, the JLH approach may be more appropriate than LMW's to model tsunamis generated by earthquake sources, since it does not implicitly assume an immediate deformation of the ocean surface. In a sense, this had to be expected since LMW developed their model in the framework of investigating tsunamis generated by underwater explosions rather than earthquakes.

Hammack (1972, eq. 3.106, p. 68) derived the following analytical solution for the sea-surface amplitude η at distance r and time t:

$$\eta(r;t) = -\zeta_0 r_0 \int_0^{+\infty} \frac{J_0(kr)J_1(kr_0)}{\cosh(kh)} \cdot \frac{\alpha^2}{\omega^2+\alpha^2} \cdot \left[e^{-\alpha t} - \cos\omega t - \frac{\omega}{\alpha}\sin\omega t\right] \cdot dk, \tag{28}$$

where ω is again given by (2).

The difference in boundary/initial conditions between the LMW and JLH models is expressed by the term $\cosh(kh)$ in the denominator of (28). For $k \to 0$, the SWA becomes justified and this term simply goes to 1, the motion at the surface being identical to the deformation of the bottom. However, outside the SWA, this term has the effect of reducing the surface displacement for a given deformation of the bottom; in simple terms, earthquake sources in the Earth are comparatively lower frequency (or red-shifted) with respect to sources at the water surface. A second difference between the two approaches is the effect of the finite duration $1/\alpha$ of the JLH source; this is expressed in (28) through the term

$$\frac{\alpha^2}{\omega^2+\alpha^2} \cdot \left[e^{-\alpha t} - \cos\omega t - \frac{\omega}{\alpha}\sin\omega t\right]. \tag{29}$$

For any time t, (29) goes to $-\cos\omega t$ when $\alpha \to \infty$, an illustration of Butkov's (1968) result that the solution of a forced linear wave equation becomes mathematically equivalent to that of an initial condition problem when the characteristic time of forcing goes to zero.

The sequencing of simulated tsunami waves computed under the JLH formalism is now examined, following the exact same strategy as with LMW solutions. An equation numbered (xx)_[yy] will refer to a substitute (xx) under JLH's formalism for eq. (yy) under LMW's. Our results are shown on Fig. 7, with the following individual fits to the critical distance r_c as a function of r_0 and h:

$$\log_{10} r_c^{(4)} = 2.505 \log_{10} r_0 + 0.041, \qquad (30)\_[6]$$

$$\log_{10} r_c^{(2)} = 2.703 \log_{10} r_0 + 0.289, \qquad (31)\_[7]$$

$$\log_{10} r_c^{(8)} = 2.002 \log_{10} r_0 + 0.253, \qquad (32)\_[8]$$

the combined data set being regressed as

$$\log_{10} r_c = 2.344 \log_{10} r_0 - 1.424 \log_{10} h + 1.110 \qquad (33)\_[9]$$

(with a global rms value of $\sigma = 0.12$ logarithmic units), which this time argues for a non-dimensional relation of the form (8) with $a \approx 1.4$.

A systematic comparison of the critical sequencing distances r_c under the LMW and JLH formalisms shows that the latter are an average of 1.87 times greater than their LMW counterparts. This is easily interpreted, as discussed above, from the conceptual differences between the two methods. The JLH solutions being generally lower frequency than the LMW ones, will exhibit less dispersion, and thus require longer ranges r to reach the critical sequencing distance r_c. However, the above ratio features a lot of scatter, varying from 1.02 (for a large plug in a shallow ocean) to 6.0 (for a small plug in a deep ocean). This is further illustrated by investigating the variation of the dominant periods T_0 at the critical distances r_c:

$$\log_{10} T_0 = 0.759 \log_{10} r_0 - 0.281 \log_{10} h + 1.866, \qquad (34a)\_[26a]$$

$$\log_{10} \omega_0 = -0.759 \log_{10} r_0 + 0.281 \log_{10} h - 1.067. \qquad (34b)\_[26b]$$

These dominant periods are found to be generally longer for the JLH model (by an average of 19 per cent compared to the LMW one), but less sensitive to the parameters r_0 and h, as expressed by gentler slopes than the theoretical values 1 and -0.5 in (34). This illustrates the fact that the wave developing under the JLH model is initially red-shifted with respect to the LMW one, and features a smoother spectrum.

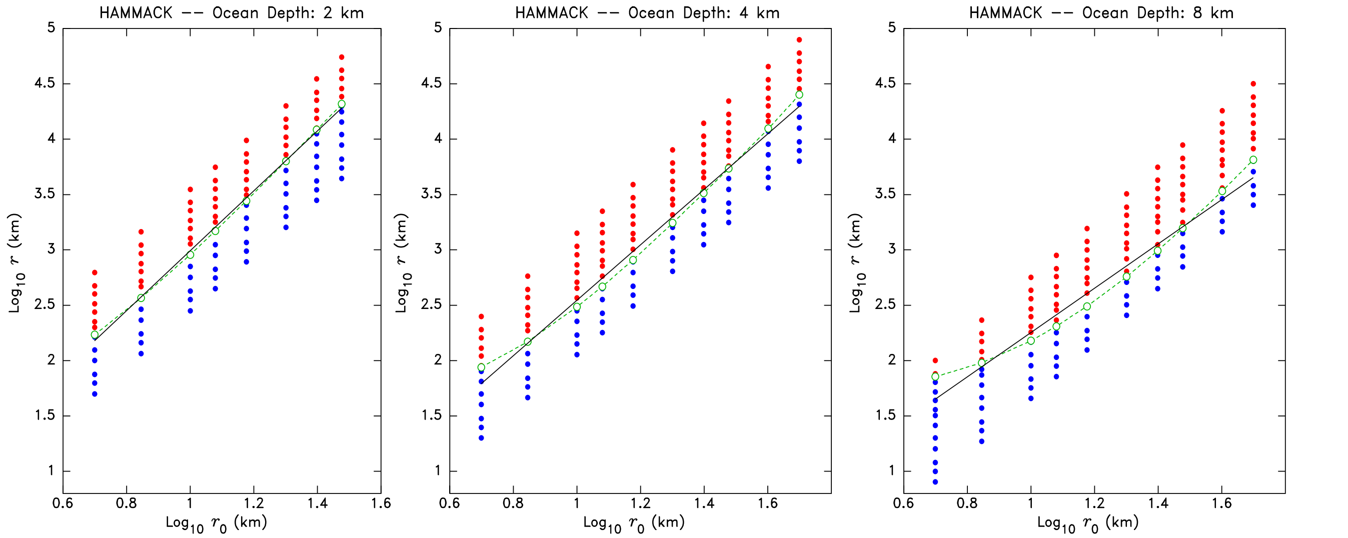

Figure 7. Same as Figs 4 and 5 for simulations under *Hammack*'s (1972) formalism.

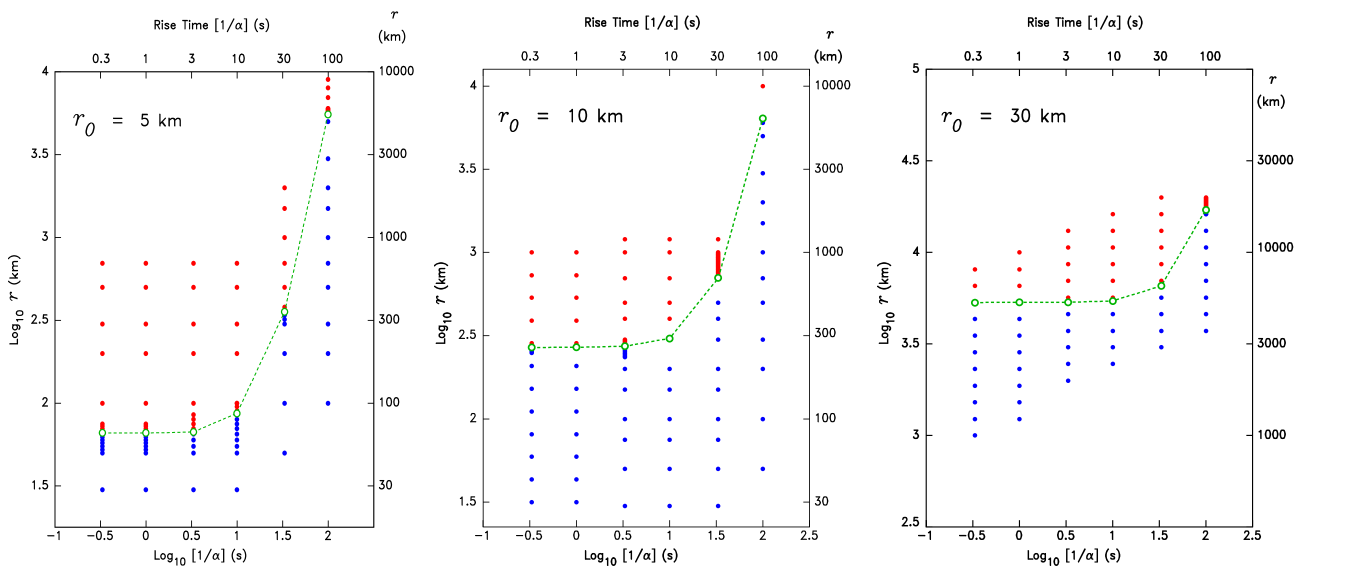

Figure 8. Influence of the parameter α on the character of JLH solutions for $h = 4$ km and $r_0 = 5$ km (left), 10 km (centre), and 30 km (right). Symbols as in Fig. 4.

Finally, on Fig. 8, we explore the influence on sequencing of the parameter α whose inverse, $1/\alpha$, represents the rise time of the source. We use three plug radii, $r_0 = 5$, 10 and 30 km, respectively, and a standard ocean depth of 4 km. We find that in all instances, α has little influence on r_c, as long as it remains large, that is, the rise time remains small. Specifically, Fig. 8 shows two regimes for r_c. For $r_0 = 5$, 10 and 30 km, r_c starts to be affected for $1/\alpha >$ 3, 6 and 20 s, respectively, suggesting that these thresholds scale with r_0, approximately as $(r_0/\sqrt{gh})/8$, an interpretation being that for small values of α, the large rise time controls the dominant frequency T_0 and hence the dispersion, while for large values of α, T_0 is controlled by the dimension of the source and is insensitive to the very short rise time.

2.4 Comparison with Glimsdal *et al.* (2013)

Our results can be compared to those of Glimsdal *et al.* (2013), who have similarly investigated the development of dispersion during propagation of tsunami waves. However, these authors consider 'space series', that is, the distribution of surface amplitude η as a function of range r, which amounts to taking a snapshot of the surface of the ocean at a given time t, while we investigate time-series $\eta(t)$ at a fixed position r. Furthermore, they consider classical dislocation sources which provide a more realistic model of tsunami generation by earthquakes, but result in a more complex two-dimensional spatial source spectrum.

In order to explore deeper the relationship between our two families of solutions, we plot on Fig. 9 space series of the LMW integral (1) for a standard depth $h = 4$ km, a source radius $r_0 = 20$ km and for times $t = 1900$ and 12 000 s. Note that we duplicate qualitatively Glimsdal *et al.*'s (2013) observations, for example, their fig. 5. For short times t, the wave is not dispersed and the maximum amplitude occurs at the wavefront. For longer times t, dispersion becomes evident, and the maximum amplitude η trails the wavefront. It is possible to define a critical time t_c separating the two regimes, which is found to be 6170 s for this combination of source parameters. Note that the critical distance r_c for the same source parameters

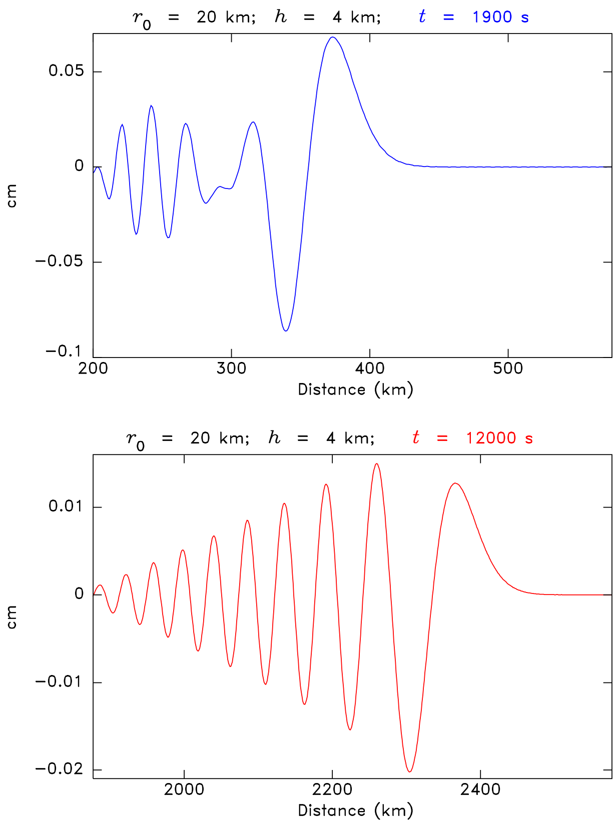

Figure 9. Space series of snapshots of the deformation η computed under LMW's formalism (5), but plotted as a function of range r, for times $t = 1900$ s (top) and $t = 12\,000$ s (bottom). Note the *MF* character for the shorter time, and the *MD* pattern for the longer one.

is predicted at 1301 km by (6), 1321 km by (9) and 1300 km by (24) and (25), which in turn would correspond to traveltimes of between 6570 and 6670 s, under the SWA. These numbers agree well with our estimate of t_c, the difference, on the order of the dominant period T_0 (430 s according to (26a) and 440 s when forcing the regression slopes to -1 and 0.5), expressing the different scope of the two formalisms (space and time-series) which are not expected to yield identical critical fields.

In conclusion, our results agree well with Glimsdal *et al.*'s (2013), even though they use a different approach and different source models.

3 SIMULATED SEQUENCING FOR REALISTIC SEISMIC SOURCES

3.1 Simulations based on the 2014 Iquique earthquake

In this section, we explore the sequencing of tsunami waves generated by a conventional seismic source. As a reference, we use the geometry of the Iquique, Chile earthquake of 2014 April 1, a moderately large event ($M_0 = 2.3 \times 10^{28}$ dyn*cm), and the last one to have generated a tsunami recorded throughout the Pacific; it featured a maximum run-up of 4.4 m in the near field. As discussed more in detail below, we will consider variants of this source to explore the influence on sequencing of the fault parameters of the event.

In all cases, we simulate the propagation of the tsunami through the entire Pacific Basin, in a spherical model of the Earth. Our simulations use the MOST code (Titov and Synolakis 1998), which solves the non-linear equations of hydrodynamics under the SWA, using a finite-difference algorithm and the method of alternating steps (Godunov 1959). MOST has been fully validated by benchmarking (Synolakis *et al.* 2008); all details can be found in Synolakis (2003).

Our reference case ('Model 1') uses the GlobalCMT solution of the Iquique earthquake ($\phi = 358^\circ$; $\delta = 12^\circ$; $\lambda = 107^\circ$). Fault parameters, listed in Table 1, were derived from the seismic moment M_0 using Geller's (1976) scaling laws. The static deformation of the ocean floor is then computed using Mansinha & Smylie's (1971) algorithm, and taken to represent the instantaneous deformation of the ocean surface at time $t = 0_+$. In order to isolate the possible influence on sequencing of bathymetry and shorelines, we initially consider an ocean of constant depth $h = 4$ km, without any islands or continents. The simulation domain is however limited to a typical Pacific Basin, covering latitudes 50°S to 62°N and longitudes 120°E to 60°W (see Fig. 10). Sequencing is investigated through the computation of times-series of sea surface height $\eta(t)$ at 677 virtual gauges distributed at regular azimuths (5°) and distances (500 km) from the source.

Fig. 10 shows typical examples of simulated *MF* and *MD* times-series, as well as a map of their distribution (note that the continents are shown only for orientation; they are absent from the model). In very general terms, the distribution of sequencing confirms the trend defined in the previous section: along a given great circle from the epicentre, wave trains are of type *MF* at short distances, and then become *MD* at greater ones. In the reference case, the transition takes place at a distance estimated at 1500 km in the lobe of directivity (we note however a strong azimuthal dependence of critical sequencing distances which will be examined below). This distance is both shorter than expected from JLH models for source radii comparable to $W/2$ (8500 km using eq. (30)), and larger than simulated by Glimsdal *et al.* (2013) in the case of the comparably sized 1969 Portuguese earthquake (estimated at few hundred kilometres by comparing the two frames in their Fig. 5; note however that the steep dip of their solution has the effect of reducing the projected width of the fault and hence of blue-shifting the spatial spectrum of their source).

The influence of source parameters on sequencing is further investigated by varying the fault dimensions. Models 2 and 3 consider sources scaled down and up, respectively, by a factor of 10 in moment, using seismic similitude laws (Geller 1976). As shown on Fig. 11, the 'SMALL' source leads to a much faster transition to type *MD*, with *MF* wave trains now constrained to a few short distances along azimuths approaching the strike of the fault, while for the 'BIG' source, the *MD* wave trains cover only a very distant range ($\geq$8500 km) in the centre of the directivity lobe. Models 4–6, investigated on Fig. 12, are obtained by artificially changing one fault dimension, outside similitude laws. Specifically, the 'WIDE' model has double the fault width of the reference model while keeping fault length and seismic slip unchanged, and thus double the seismic moment, the 'THIN' model has half the width (and the same length) for half the seismic moment, and the 'LONG' one double the length and the same width, for double the seismic moment. Fig. 12 confirms that the development of sequencing varies significantly with the dimensions of the fault.

A simple interpretation of these trends can be given as follows. Motivated by the results in Section 2, we assume that the critical sequencing distance for a tsunami generated by a rectangular source of dimensions length L and width W is controlled by the dominant wavelength (or period) of the tsunami, which in turn results from a condition of positive interference among the wavelets generated at

Table 1. Parameters of models used in numerical simulations.

Model number	Name	Ocean model	Moment M_0 (10^{28} dyn*cm)	Fault length (km)	Fault width (km)	Slip (m) (km)
		Reference event: Iquique, 2014 April 1 ($\phi = 358°$; $\delta = 12°$; $\lambda = 107°$)				
1	REFERENCE	Flat, No conts.	2.3	147	74	4.3
2	SMALL	Flat, No conts.	0.23	68	34	2.0
3	BIG	Flat, No conts.	23.	317	158	9.3
4	WIDE	Flat, No conts.	4.6	147	147	4.3
5	THIN	Flat, No conts.	1.2	147	37	4.3
6	LONG	Flat, No conts.	4.6	298	74	4.3
7	TRUE BATHY	True bathymetry	2.3	147	74	4.3
		Maule, Chile, 2010 February 27 ($\phi = 16°$; $\delta = 14°$; $\lambda = 104°$)				
8	MAULE	Flat, No conts.	19.8	400	112	9.0
9	MAULE	True bathymetry	19.8	400	112	9.0
		Tohoku, Japan, 2011 March 11 ($\phi = 193°$; $\delta = 14°$; $\lambda = 81°$)				
10	TOHOKU	Flat, No conts.	39.5	350	80	28.3
11	TOHOKU	True bathymetry	39.5	350	80	28.3

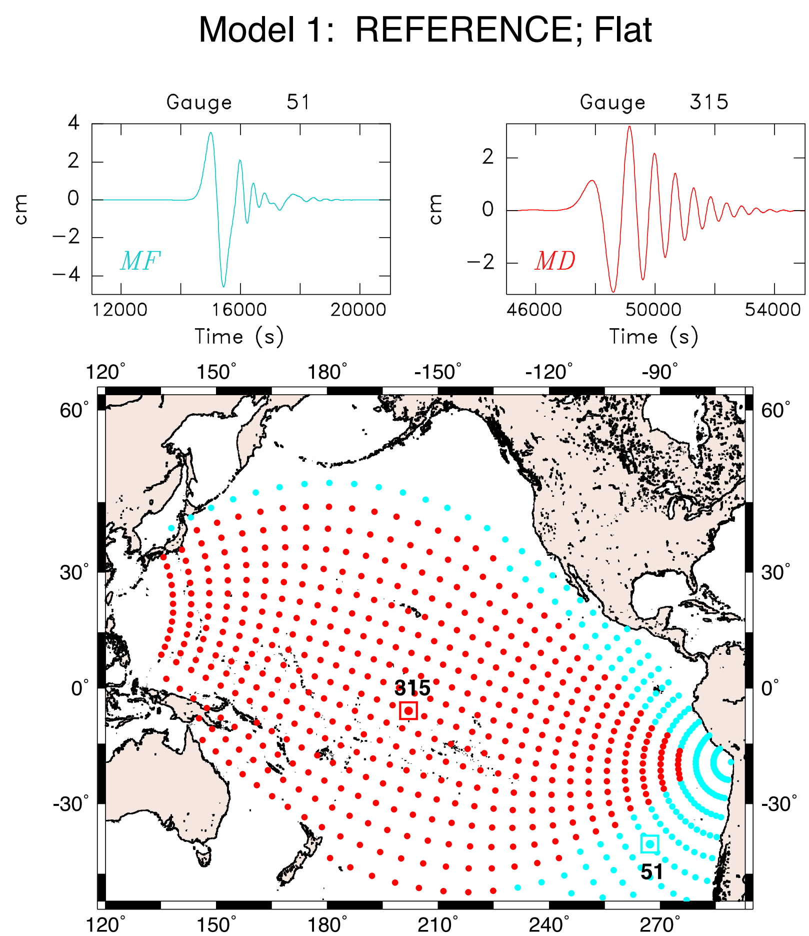

Figure 10. MOST simulations for the earthquake reference source (2014 Iquique earthquake; Model 1). Top: examples of *MF* and *MD* wave trains. Bottom: distribution of virtual gauges, colour-coded according to nature of sequencing (*MF* in blue; *MD* in red). The locations of Gauges 51 and 315, illustrated in the top frames, are outlined. Note that this simulation involves a totally flat ocean bottom; the continents are absent from the model and are drawn here only for orientation. See the text for details.

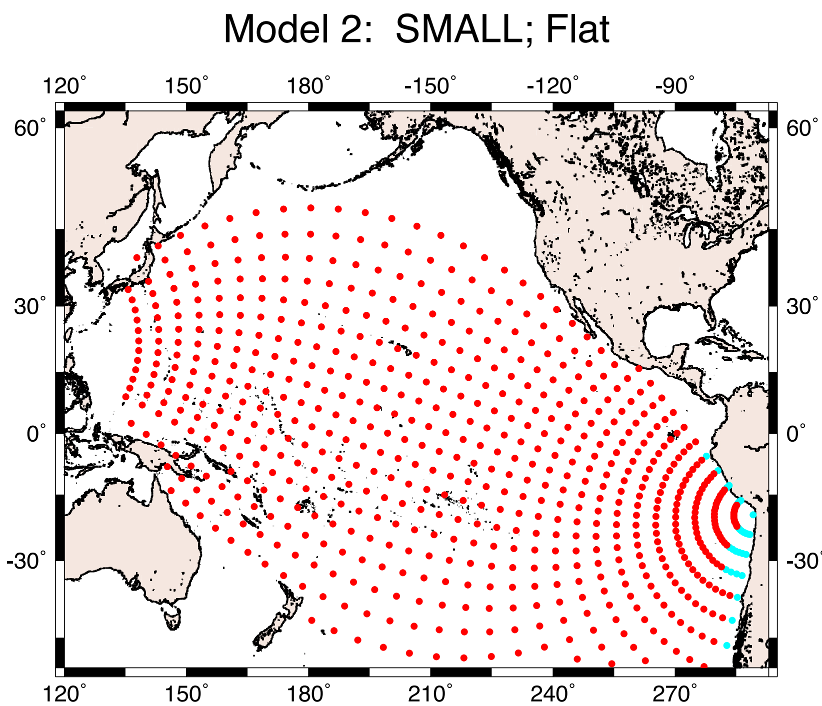

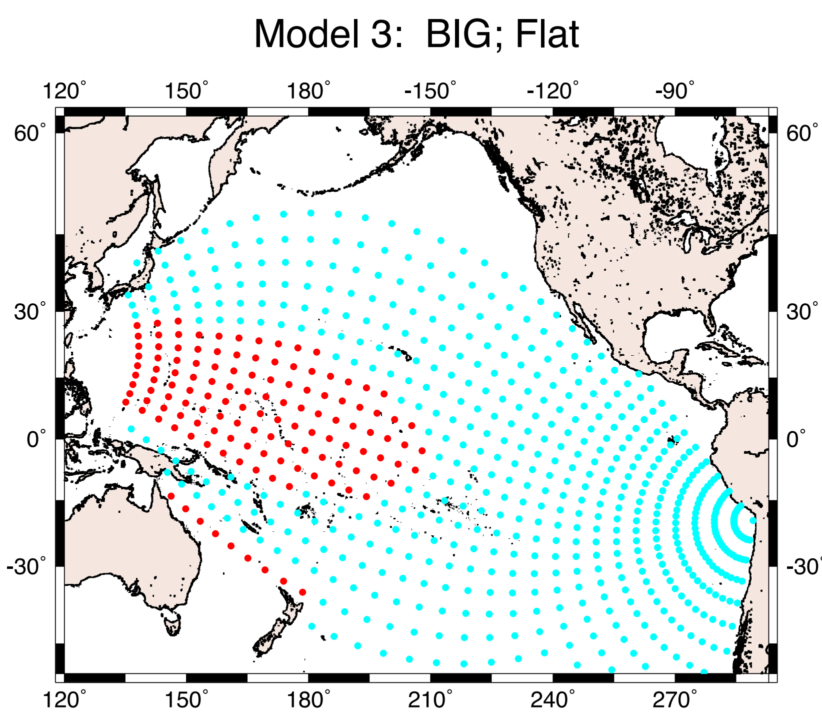

Figure 11. Distribution of *MF* (blue) and *MD* (red) simulated time-series generated by Models 2 ('SMALL'; top) and 3 ('BIG'; bottom), for a flat ocean bottom with no continents.

the various elements of the fault plane, as described conceptually by Ben-Menahem & Rosenman (1972). Following Yamashita & Sato (1974) and more recently Rabinovich (1997), we expect the fundamental dominant period to be given by

$$T = \frac{2D}{\sqrt{gh}}, \tag{35}$$

where D is a critical fault dimension controlling constructive interference. In the axis of the lobe of directivity, that is, at right angle from the fault strike, $D = W \cos\delta$, where W is the fault width and δ the dip angle of the fault, as verified, for example, by Abe (2006) in the case of the 2004 Sumatra tsunami. For a shallow dipping thrust event, $D \approx W$. As W (hence D) increases, the dominant wavelength will increase, and so will the critical sequencing distance, which it controls. Moving in azimuth away from the directivity lobe, the apparent size of the source in the direction of propagation will increase (we have verified that indeed, the dominant period T in the simulated tsunami time-series increases), with the result that the critical

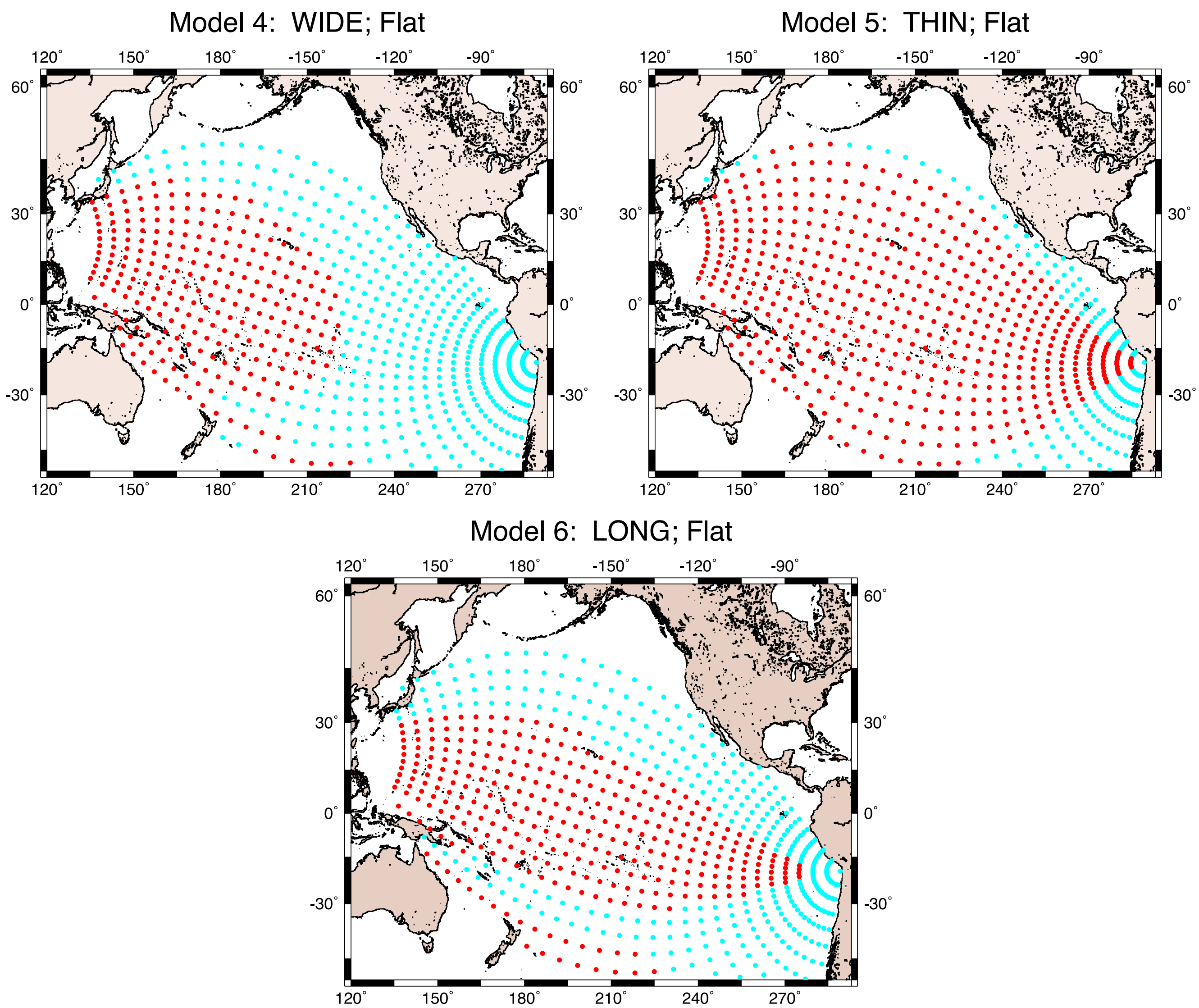

Figure 12. Same as Fig. 11 for Models 4 ('WIDE'; top left), 5 ('THIN'; top right) and 6 ('LONG'; bottom).

sequencing range will increase as well. By contrast, the effect of the fault length L would be concentrated in the direction of faulting, which does not sample the open ocean in real-life situations in the Pacific Basin. These simple arguments explain, at least qualitatively, the main characteristics of the sequencing patterns expressed on Figs 10–12, namely the growth of the critical sequencing range with width W, less so with length L, and with increasing azimuth away from the centre of the directivity lobe.

We next consider in Model 7 the same source as in Model 1, that is, the reference 2014 Iquique earthquake, but run the simulation for the real bathymetry of the Pacific Basin, including its continental and island shores. As shown on Fig. 13, the distribution of *MF* versus *MD* waveforms follows the same trend as for the flat bottom case (Fig. 10), that is a transition to the *MD* regime at greater ranges, but the pattern is somewhat more erratic, with small-scale heterogeneities probably expressing the influence of secondary arrivals due to refraction by regional bathymetric features. We also note that the transition within the lobe of directivity takes place at a significantly greater range; this reflects the young age and hence the shallow depth of the Pacific floor in the Nazca plate, and would agree, at least qualitatively, with the dependence of r_c on h derived in eq. (24).

3.2 The case of the two major 2010 Maule and 2011 Tohoku tsunamis

Finally, on Fig. 14, we show the distribution of sequencing for simulations of the two large events of 2010 (Maule, Chile, *left*) and 2011 (Tohoku, Japan, *right*). For a flat bathymetry without continents (*top*), the general characteristics of our previous models are reproduced, with the *MD* patterns developing only at large ranges ($\geq$7500 and 4000 km, respectively), in the lobe of the radiation pattern, the smaller critical range for the Tohoku tsunami expressing the more compact dimensions of its source. The patterns become more scattered in the case of the real bathymetry (*bottom*), with a lessening of the azimuthal impact and an opposite effect on critical range: the latter is generally increased significantly for the Maule event (as it was for the Iquique event—see Figs 10 and 13), but remains essentially unchanged in the Tohoku case. This disparity is

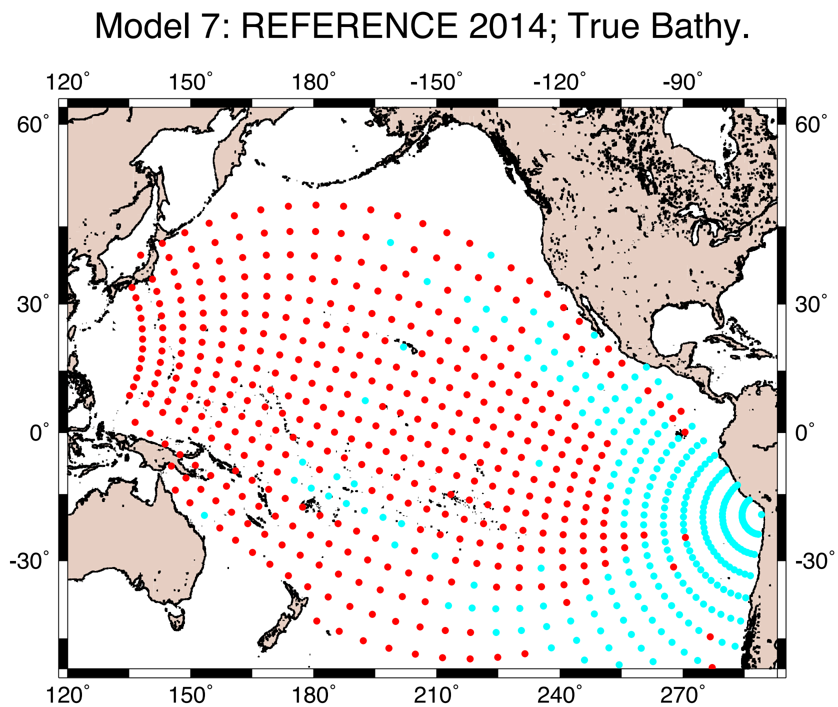

Figure 13. Distribution of virtual gauges, colour-coded according to nature of sequencing (*MF* in blue; *MD* in red) for the reference Iquique earthquake source, using the real bathymetry of the Pacific Basin, continents and islands.

tentatively explained by the presence of shallow bathymetry, leading to longer ranges r_c according to (24), along the early parts of the Maule paths in the Nazca plate and across the East Pacific Rise, as compared to deep and relatively smooth bathymetry in the Western Pacific in the Tohoku case.

On Fig. 14, we re-plot the individual DART measurements compiled on Fig. 2, allowing for a direct evaluation of the success of our simulations in predicting sequencing as recorded in real life. For the Maule event, the flat-bottom, no-continents Model 8 correctly predicts 10 out of 16 gauges, with 4 clear violations, one DART gauge at the boundary between the two regimes, and one in an area where no virtual gauges were deployed. In Model 9, using real bathymetry, 14 out of 16 are correctly predicted, with still one gauge at the regime boundary (incidentally, reversed from Model 8) and one uncovered. For the Tohoku tsunami, Model 10 (flat) correctly predicts 15 out of 24, with eight clear violations and one gauge close to the pattern boundary. Under Model 11 (with real bathymetry), these numbers become 15 correct predictions and 9 gauges at pattern boundaries.

While the match between predicted and observed sequencing is not perfect, it is however highly satisfactory, since most of our unpredicted gauges are located near the boundaries of sequencing regime, where the eventual pattern (*MD* versus *MF*) may be controlled by subtle small-scale heterogeneities in bathymetry. This is clearly the case for the lone gauges wrongly predicted in Model 9, where the pattern of sequencing is inverted at the Kermadec DART site with respect to the flat-bottom Model 8. In the less satisfactory case of the 2011 Tohoku tsunami, we note that our simulation uses a simplified model of earthquake rupture featuring a homogeneous slip on the fault. A more sophisticated model, taking into account the strongly heterogeneous seismic slip featured by this event (e.g. Ammon *et al.* 2011; Fujii *et al.* 2011) would result in blue-shifting of the wavefield, which in turn would predict a stronger dependence on small-scale bathymetry.

As a conclusion of our set of simulations, we present on Fig. 15 the time-series simulated under Model 11 at virtual gauge 450, the closest one to the island of Tahiti, where Fig. 1 was obtained. While not reproducing all the details of the maregram in Fig. 1, it clearly qualifies as an *MD* pattern, and the time lag between the arrival of the first wave and the absolute maximum (one hour) compares favourably with the observation on Fig. 1.

We emphasize that a detailed comparison between Figs 1 and 15 is not warranted, in view of a number of simplifications inherent in our simulation: gauge 450 (20.55°S; 150.06°W) is located 330 km South of Papeete, which remains within a typical wavelength of the main wave packet; however the record on Fig. 1 was obtained at a maregraph located in Papeete harbour, where the water depth is estimated at 20 m (Reymond *et al.* 2012). Despite the fact that Papeete harbour features a relatively simple topography and thus does not lend itself to extreme non-linear amplification of tsunami waves, a detailed simulation of the record on Fig. 1 would require fine-scale resolution of the local bathymetry around the island of Tahiti, and into the harbour itself, as well as a similarly finer local computational grid, and thus transcends the scope of this paper, which is simply to identify the physical parameters controlling the evolution of sequencing. In this context, our comparison of Figs 1 and 15 simply serves the purpose of confirming that the general physical agents identified in the previous sections as controlling the evolution of sequencing remain the main contributors to the late arrival of the maximum amplitude in Papeete during the 2011 tsunami, as experienced by the first author under operational conditions.

Finally, we note that the general evolution from *MF* to *MD* scenarios as distance increases was specifically identified by Rabinovich & Thomson (2007) on a data set of tidal gauge records of the 2004 Sumatra–Andaman tsunami. However, as mentioned above, such records can be strongly affected by the non-linearity of these

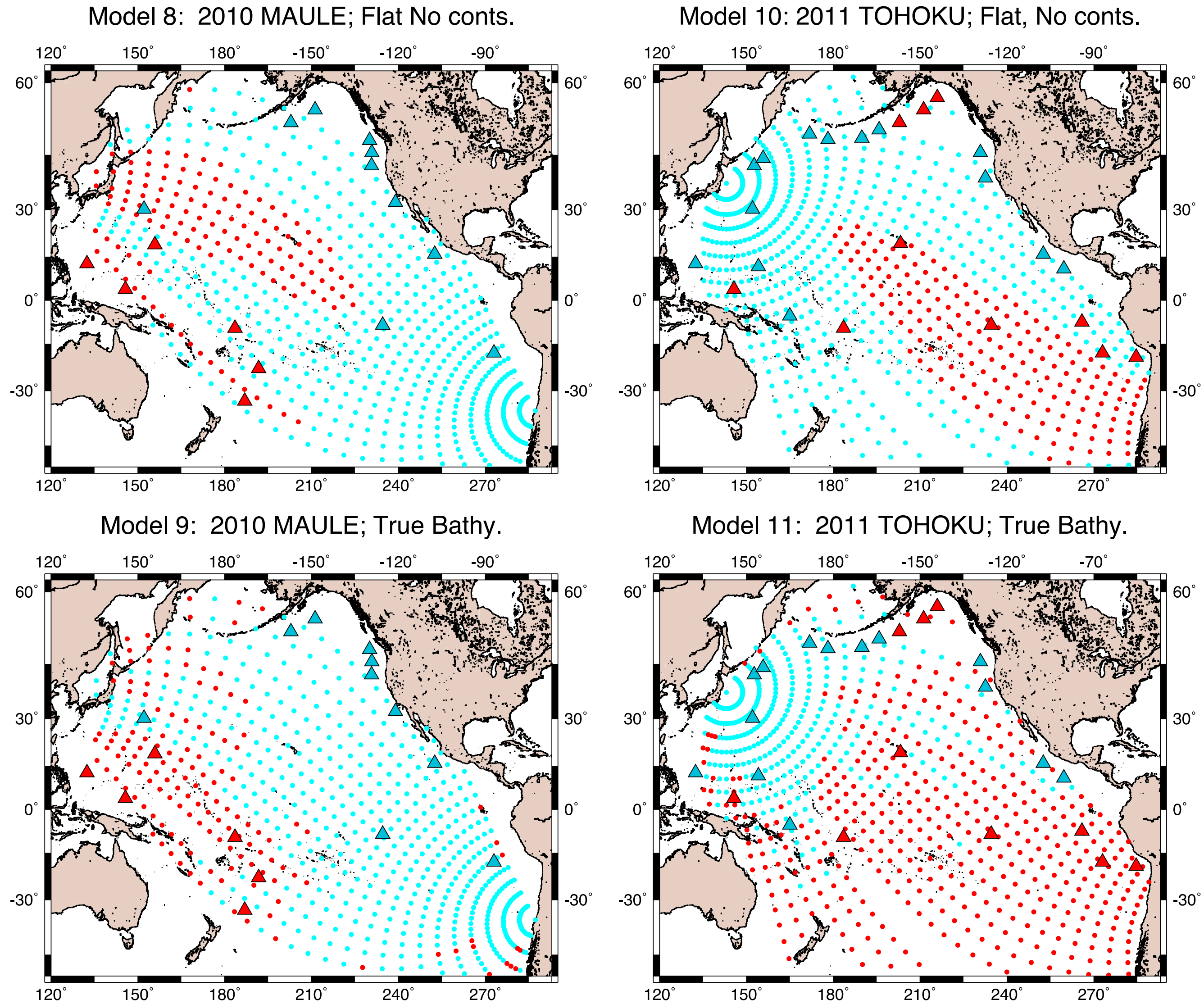

Figure 14. Simulations of the 2010 Maule (left) and 2011 Tohoku (right) using a flat bathymetry with no continents (top) and the real Pacific Basin bathymetry (bottom). Sequencing at each virtual gauge is shown in blue (*MF*) or red (*MD*). Superimposed on each frame are the data recorded at DART buoys from Fig. 2 (triangles).

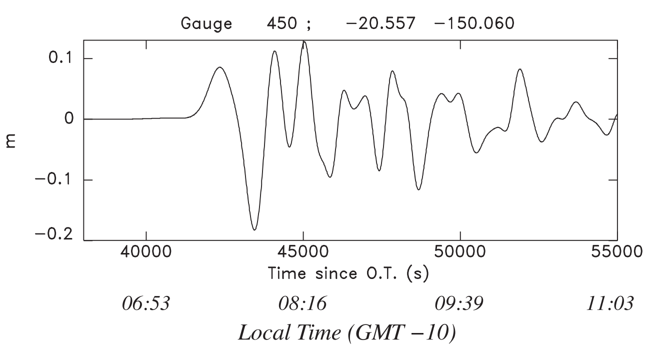

Figure 15. Simulation under Model 11 (Tohoku tsunami; real bathymetry) at virtual gauge 450, closest to Papeete, Tahiti.

instruments, and by the response of the harbours where they are deployed. Nevertheless, our results suggest that the main origin of this evolution in sequencing in the 2004 data set is attributable to dispersion.

3.3 Validating the use of MOST

All above simulations were carried out using the MOST algorithm, which is intrinsically non-dispersive, since it solves the equations of hydrodynamics under the SWA. In this respect, it may appear surprising that this algorithm, when used with a flat-bottom ocean eliminating the effects of focusing and multipathing, should be capable of reproducing the general trends of sequencing patterns defined in Section 2, and attributed to the effect of dispersion expressed by (2) outside the SWA.

This apparent paradox is resolved in the framework of Burwell *et al.*'s (2007) discussion of the numerical diffusion and dispersion induced into the MOST algorithm by the process of discretization. These authors show that the process is controlled by the ratio:

$$\beta^{\mathrm{BTC}} = \sqrt{gh} \cdot \frac{\Delta t}{\Delta x}, \tag{36}$$

where Δt and Δx are the temporal and spatial sampling rates, respectively (we use the notation β^{BTC} to represent these authors' parameter β, since it is unrelated to β defined in eq. (21)). We recall that the Courant–Friedrichs–Lewy stability condition requires $\beta^{\mathrm{BTC}} < 1$ (Courant *et al.* 1928); in the present simulations, we use values β^{BTC} varying from 0.5 (for latitudinal steps and equatorial regions) to 0.9 for longitudinal steps at high latitudes; an average of $\beta^{\mathrm{BTC}} = 0.7 \approx 1/\sqrt{2}$ allows a direct comparison with Burwell *et al.*'s (2007) fig. 11, which shows that the artificial numerical dispersion in MOST reproduces the theoretical dispersion (2) of linear wave theory outside the SWA, for all wavenumbers satisfying $k \cdot \Delta x \leq 1.5$, or in the case of our simulations, wavelengths greater than about 15 km, or periods greater than 75 s, which is clearly the case of all legitimate seismic sources of transoceanic tsunamis. This explains why MOST simulations can effectively predict the sequencing patterns shown in Section 2 to evolve from dispersive effects. In this context, the comparison of the top and bottom frames of Fig. 14 shows that the development of *MD* patterns cannot be simply attributed to irregularities in bathymetry.

4 CONCLUSION

Our examination of hypothetical solutions comprising both instantaneous circular surface sources and time-dependent seafloor displacements has established the existence of a critical distance r_c at which sequencing of tsunami waves in the far-field transitions from an '*MF*' pattern in which the maximum sea surface amplitude is carried by the first arriving leading elevation, into an '*MD*' waveshape where the maximum crest is delayed until a later oscillation in the primary wave packet. In the simplified case of cylindrical waves generated by an instantaneous 'top-hat' uplift of the ocean surface, we have derived the simple expression

$$r_c = 2.60 \cdot \frac{r_0^3}{h^2} \tag{37}$$

for scaling r_c to source radius r_0 and ocean depth h. This expression can be justified by assuming that sequencing derives from frequency dispersion inside the primary wave packet, as the width of its spectrum around its dominant period T_0 becomes dispersed in time in an amount comparable to T_0, the latter being itself controlled by a combination of source size r_0 and ocean depth h.

In very simple terms, the power law exponents (3 and 2) in (37) may be understood by noting that it can be rewritten as

$$r_c = \frac{\beta}{\delta} \cdot \Lambda_0 \cdot \frac{1}{\xi_0^2}, \tag{38}$$

where the denominator ξ_0^2 is, according to (17), a measure of the relative effect of dispersion on the group velocity, at the dominant wavelength Λ_0; then r_c scales directly with Λ_0 (and hence r_0), divided by this non-dimensional parameter.

In the case of sources rapidly uplifting the ocean floor, the critical distance r_c remains comparable to (37) for rapid sources, but becomes larger for slower sources, reflecting the general red-shifting of the wave's spectrum.

Models involving realistic earthquake sources confirm the transition from *MF* patterns to *MD* ones at larger ranges, with fault width W having a greater influence than fault length L on the critical distance and propagation outside the lobe of directivity further increasing the critical distance. The presence of laterally variable bathymetry, including continent and islands, further affects the sequencing of tsunami waves in the far field by generating focusing, defocusing and multipathing of tsunami rays in the oceanic basin, without however modifying the main patterns of the sequencing distribution.

Simulations of the two largest recent transoceanic tsunamis (2010 Maule, Chile and 2011 Tohoku, Japan) reveal similar patterns, and accurately predict the distribution of sequencing at the majority of the DART buoys having recorded these two events, which incidentally confirms that delayed arrivals observed at coastal stations are not (or at least not entirely) due to site effects involving the non-linear response of bays and harbours. Our 2011 simulation at the virtual gauge closest to Papeete also predicts an *MD* pattern, with an absolute maximum delayed on the order of one hour, as recorded in real time by the harbour maregraph.

In this context, we stress that our results do not necessarily imply that the sequencing transition from *MF* to *MD* regimes will change inundation amplitudes estimated by codes solving non-linear shallow water equations, if their numerical characteristics are similar to those used, for example, by the MOST algorithm, as also argued by Synolakis & Kânoğlu (2015). We note in particular that the amplitude of the delayed maximum at the tidal gauge record shown on Fig. 1 (and acceptably reproduced on Fig. 15) had been correctly predicted under operational conditions based on algorithms using SWA codes (Reymond *et al.* 2013).

While not pretending to explain all details of the time-series recorded in the far field from a major tsunami, our study provides a theoretical framework identifying the main agents governing the evolution from maximum first to maximum delayed regimes, in the context of the scaling of the seismic source. From an operational standpoint, it brings analytical support to the need for a precautionary attitude in emergency management, re-emphasizing that arrival times announced as part of tsunami warning dispatches refer to the initiation of the phenomenon, while its full development may delay the most dangerous parts of the wave for a few hours. Populations at risk must be educated in this respect, if one is to prevent repeating the tragedies in Hilo (1960) or Crescent City (1964).

ACKNOWLEDGEMENTS

CES acknowledges partial support from the National Science Foundation under grant CMI-15-38624 to the University of Southern California and from Project ASTARTE funded under the 7th Framework Programme for Research and Technological Development of the European Union, under grant 603839 to the Technical University of Crete. EAO acknowledges partial support from the National Science Foundation under subcontract from the University of Pittsburgh's grant number OCE-13-31463. The paper was significantly improved by the comments of Alexander Rabinovich and another reviewer.

REFERENCES

Abe, K., 2006. Dominant periods of the 2004 Sumatra tsunami and the estimated source size, *Earth Planet Space,* **58,** 217–221.

Admire, A.R., Dengler, L.A., Crawford, G.B., Uslu, B.U., Borrero, J.C., Greer, S.D. & Wilson, R.I., 2014. Observed and modeled currents from the Tohoku-oki, Japan and other recent tsunamis in Northern California, *Pure appl. Geophys.,* **171,** 3385–3403.

Ammon, C.J., Lay, T., Kanamori, H. & Cleveland, M., 2011. Rupture model of the 2011 off the Pacific coast of Tohoku earthquake, *Earth Planet Space,* **63,** 693–696.

Ben-Menahem, A. & Rosenman, M., 1972. Amplitude patterns of tsunami waves from submarine earthquakes, *J. geophys. Res.,* **77,** 3097–3128.

Burwell, D., Tolkova, E. & Chawla, A., 2007. Diffusion and dispersion characterization of a numerical tsunami model, *Ocean Model.,* **19,** 10–30.

Butkov, E., 1968. *Mathematical Physics,* 735 pp., Addison-Wesley.

Courant, R., Friedrichs, K. & Lewy, H., 1928. Über die partiellen Differenzengleichungen der mathematischen Physik, *Math. Ann.,* **100,** 32–74.

Eaton, J.P., Richter, D.H. & Ault, W.U., 1961. The tsunami of May 23, 1960, on the Island of Hawaii, *Bull. seism. Soc. Am.,* **51,** 135–157.

Fujii, Y., Satake, K., Sakai, S., Shinohara, M. & Kanazawa, T., 2011. Tsunami source of the 2011 off the Pacific coast of Tohoku earthquake, *Earth Planet Space,* **63,** 815–820.

Geller, R.J., 1976. Scaling relations for earthquake source parameters and magnitudes, *Bull. seism. Soc. Am.,* **66,** 1501–1523.

Glimsdal, S., Pedersen, G.K., Harbitz, C.B. & Løvholt, F., 2013. Dispersion of tsunamis: does it really matter?, *Nat. Haz. Earth Syst. Sci.,* **13,** 1507–1526.

Godunov, S.K., 1959. Finite difference methods for numerical computations of discontinuous solutions of the equations of fluid dynamics, *Mat. Sb.,* **47,** 271–295.

Hammack, J.L., 1972. Tsunamis—a model of their generation and propagation, *PhD dissertation,* Calif. Inst. Tech., Pasadena, 261 pp.

Kajiura, K., 1963. The leading wave of a tsunami, *Bull. Earthq. Res. Inst. Tokyo Univ.,* **41,** 535–571.

Kowalik, Z., Knight, W., Logan, T. & Whitmore, P., 2005. Numerical modeling of the global tsunami: Indonesian tsunami of 26 December 2004, *Sci. Tsunami Haz.,* **23,** 40–56.

Le Méhauté, B. & Wang, S., 1995. *Water Waves Generated by Underwater Explosion,* 367 pp., World Scientific.

Mansinha, L. & Smylie, D.E., 1971. The displacement fields of inclined faults, *Bull. seism. Soc. Am.,* **61,** 1433–1440.

Mirchina, N.R. & Pelinovsky, E.N., 1980. Asymptotic forms of wave motions on the surface a liquid, *Izv. Atmos. Ocean. Phys.,* **16,** 637–639.

Mirchina, N.R. & Pelinovsky, E.N., 1982. Nonlinear and dispersive effects for tsunami waves in the open ocean, *Sci. Tsunami Haz.,* **2**(4), D-1–D-9.

Mirchina, N.R., Pelinovsky, E.N. & Shavratsky, S.Kh., 1982. Parameters of tsunami waves in the source, *Sci. Tsunami Haz.,* **2**(6), B-1–B-7.

National Research Council, 1970. The great Alaska earthquake of 1964, in *Human Ecology,* U.S. Nat. Acad. Sci., Washington, DC, 510 pp.

Okal, E.A., Fritz, H.M., Raveloson, R., Joelson, G., Pančošková, P. & Rambolamanana, G., 2006. Madagascar field survey after the December 2004 Indian Ocean tsunami, *Earthq. Spectra,* **22,** S263–S283.

Rabinovich, A.B., 1997. Spectral analysis of tsunami waves: Separation of source and topography effects, *J. geophys. Res.,* **102,** 12 663–12 676.

Rabinovich, A.B. & Thomson, R.E., 2007. The 26 December 2004 Sumatra tsunami: analysis of the tide gauge data from the world ocean, Part 1: Indian Ocean and South Africa, *Pure appl. Geophys.,* **164,** 261–308.

Rabinovich, A.B., Stroker, K., Thomson, R.E. & Davis, E., 2011. DARTs and CORK in Cascadia Basin: high-resolution observations of the 2004 Sumatra tsunami in the northeast Pacific, *Geophys. Res. Lett.,* **38**(8), L08607, doi:10.1029/2011GL047026.

Reymond, D., Okal, E.A., Hébert, H. & Bourdet, M., 2012. Rapid forecast of tsunami wave heights from a database of pre-computed simulations, and application during the 2011 Tohoku tsunami in French Polynesia, *Geophys. Res. Lett.,* **39**(11), L11603, doi:10.1029/2012GL051640.

Reymond, D., Hyvernaud, O. & Okal, E.A., 2013. The 2010 and 2011 tsunamis in French Polynesia: operational aspects and field surveys, *Pure appl. Geophys.,* **170,** 1169–1187.

Shevchenko, G., Ivelskaya, T., Loskutov, A. & Shishkin, A., 2013. The 2009 Samoa and 2010 Chilean tsunamis recorded on the Pacific coast of Russia, *Pure appl. Geophys.,* **170,** 1511–1527.

Synolakis, C.E., 2003. Tsunami and seiche, in *Earthquake Engineering Handbook,* pp. 9-1–9-90, eds Chen, W.-F. & Scawthron, C., CRC Press.

Synolakis, C.E. & Kânoğlu, U., 2015. The Fukushima accident was preventable, *Phil. Trans. R. Soc. A,* **373,** doi:10.1098/rsta.2014.0379.

Synolakis, C.E., Bernard, E.N., Titov, V.V., Kânoğlu, U. & González, F.I., 2008. Validation and verification of tsunami numerical models, *Pure appl. Geophys.,* **165,** 2197–2228.

Tadepalli, S. & Synolakis, C.E., 1996. Model for the leading waves of tsunamis, *Phys. Rev. Lett.,* **77,** 2141–2145.

Titov, V.V. & González, F.I., 1997. Implementation and testing of the Method Of Splitting Tsunami (MOST) model, *NOAA Tech. Memo,* ERL-PMEL **112**, NOAA Pacific Marine Environ. Lab., Seattle.

Titov, V.V. & Synolakis, C.E., 1998. Numerical modeling of tidal wave runup, *J. Waterw. Port Coast. Ocean Eng.,* **124,** 157–171.

Titov, V.V., Rabinovich, A.B., Mofjeld, H., Thomson, R.E. & González, F.I., 2005. The global reach of the 26 December 2004 Sumatra tsunami, *Science,* **309,** 2045–2048.

Yamashita, T. & Sato, R., 1974. Generation of tsunami by fault model, *J. Phys. Earth,* **22,** 415–1440.